RSC Advances

Thermal conductivity of monolayer MoS2, MoSe2, and WS2: Interplay of mass effect, interatomic bonding and anharmonicity

Journal:	*RSC Advances*
Manuscript ID	RA-ART-09-2015-019747.R1
Article Type:	Paper
Date Submitted by the Author:	15-Dec-2015
Complete List of Authors:	Peng, Bo; Fudan University, Department of Optical Science and Engineering Zhang, Hao; Fudan University, Department of Optical Science and Engineering Shao, Hezhu; Chinese Academy of Sciences, Ningbo Institute of Materials Technology and Engineering Xu, Yuchen; Fudan University, Department of Optical Science and Engineering Zhang, Xiangchao; Fudan University, Department of Optical Science and Engineering Zhu, Heyuan; Fudan University, Department of Optical Science and Engineering
Subject area & keyword:	Nanomaterials - Nanoscience < Nanoscience

Journal Name

ARTICLE TYPE

Cite this: DOI: 10.1039/xxxxxxxxxx

Thermal conductivity of monolayer MoS_2, $MoSe_2$, and WS_2: Interplay of mass effect, interatomic bonding and anharmonicity

Bo Peng[1], Hao Zhang*[1], Hezhu Shao[2], Yuchen Xu[1], Xiangchao Zhang[1] and Heyuan Zhu[1]

Received Date
Accepted Date

DOI: 10.1039/xxxxxxxxxx

www.rsc.org/journalname

Phonons are essential for understanding the thermal properties in monolayer transition metal dichalcogenides. We investigate the lattice dynamics and thermodynamic properties of MoS_2, $MoSe_2$, and WS_2 by first principles calculations. The obtained phonon frequencies and thermal conductivities agree well with the measurements. Our results show that the thermal conductivity of MoS_2 is highest among the three materials due to its low average atomic mass. We also discuss the competition between mass effect, interatomic bonding and anharmonic vibrations in determining the thermal conductivity of WS_2. Strong covalent W-S bonding and low anharmonicity in WS_2 are found to be crucial in understanding its much higher thermal conductivity compared to $MoSe_2$.

1 Introduction

Monolayer transition metal dichalcogenides, MX_2 (M = Mo, W; X = S, Se), have aroused much interest recently due to their remarkable properties for applications in next-generation nanoelectronic and energy conversion devices[1–3]. Monolayer MX_2 field-effect transistors are expected to have high on/off ratio due to the band gap of 1.0-2.0 eV[4–6]. Theoretical calculations have predicted an indirect to direct bandgap transition when the MX_2 crystal is thinned to monolayer, which provides new opportunities for engineering the electronic structure of MX_2 at the nanoscale[7,8]. Furthermore, the band gap of monolayer MX_2 can be tuned reversibly by biaxial strain and is subsequently able to capture a broad range of the solar spectrum[9,10]. Besides these remarkable properties, monolayer MX_2 is also a promising material for spintronics and valleytronics[2,11]. Since all these applications are closely related to its thermal properties, it is necessary to investigate the lattice dynamics and thermodynamic properties of MX_2. For instance, high-performance electronic devices strongly depend on high thermal conductivity for highly efficient heat dissipation, while low thermal conductivity is preferred in thermoelectric application.

In semiconductors, heat is carried by the atomic vibrations that are quantized as phonons[12]. Theoretical predictions based on the phonon Boltzmann transport equation have found that monolayer WS_2 has the highest thermal conductivity (142 W/mK) at room temperature, then followed by MoS_2 (103 W/mK) and $MoSe_2$ (54 W/mK)[13]. However, the measured thermal conductivities for monolayer MoS_2 and WS_2 are 34.5 ± 4 W/mK[14] and 32 W/mK[15], respectively, which are inconsistent with the theoretical predictions. Furthermore, various phonon properties such as interatomic bonding and anharmonic vibrations, and their roles in heat transport, still lack a unified understanding. The parameters that affect phonon transport include crystal structure, atomic mass, interatomic bonding, and anharmonicity[16–18]. Generally there are four rules for finding a nonmetallic crystal with high thermal conductivity, including (i) low average atomic mass, (ii) strong interatomic bonding, (iii) simple crystal structure, and (iv) low anharmonicity[16]. All monolayer MX_2 compounds have similar crystal structures, while conditions (i) and (ii) imply a large Debye temperature, and condition (iv) means small Grüneisen

[1] *Shanghai Ultra-precision Optical Manufacturing Engineering Center, Department of Optical Science and Engineering, Fudan University, Shanghai 200433, China*
[2] *Ningbo Institute of Materials Technology and Engineering, Chinese Academy of Sciences, Ningbo 315201, China*
E-mail: zhangh@fudan.edu.cn

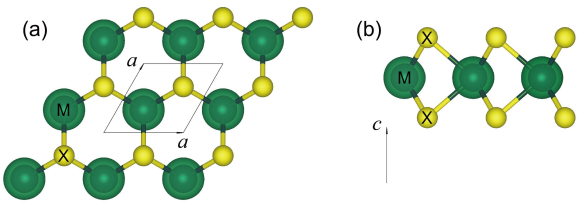

Fig. 1 (a) Top view and (b) side view of crystal structure of monolayer MX_2. The primitive vectors are **a**$(a,0,0)$, **b**$(a/2,\sqrt{3}a/2,0)$, and **c**$(0,0,c)$.

parameter, which altogether lead to a high thermal conductivity according to the Slack's theory[16].

Recent theoretical investigations have provided a quantitative analysis of the roles of mass, structure, bond strength and anharmonicity in thermal expansion and thermomechanics of MX_2 and other 2D materials such as graphene[19–22]. However, the roles of mass, interatomic bonding, and anharmonic vibrations in phonon transport still remain uninvestigated. Clear knowledge of the underlying physics will be helpful for understanding and modulating the thermal transport in MX_2, for example, through doping other M or X atoms such as $Mo_{1-x}W_xS_2$ and $MoS_{2(1-x)}Se_{2x}$[23,24].

Here we investigate fundamental vibrational properties to understand phonon transport in MoS_2, $MoSe_2$ and WS_2. The measured phonon frequencies are well reproduced in our calculations. The thermodynamic properties are calculated within quasiharmonic approximation, and the calculated thermal conductivities agree well with the measurements. Combining first principles calculations and the Slack model, the roles of mass, interatomic bonding, and anharmonicity in thermal transport are clearly revealed.

2 Methodology

All calculations are implemented in the Vienna *ab initio* simulation package (VASP) based on the density functional theory (DFT) method[25]. The Perdew, Burke, and Ernzerhof (PBE) parametrization within the generalized gradient approximation (GGA) is used for the exchange-correlation functional. A plane-wave basis set is employed with the kinetic energy cutoff of 600 eV. A $15\times15\times1$ **k**-mesh is used during structural relaxation for the unit cell until the energy differences are converged within 10^{-6} eV, with a Hellman-Feynman force convergence threshold of 10^{-4} eV/Å. We maintain the interlayer vacuum spacing larger than 12 Å to eliminate the interaction with periodic boundary condition.

In the calculation of phonon dispersion, the harmonic interatomic force constants (IFCs) are obtained by density functional perturbation theory (DFPT) using the supercell approach, which calculates the dynamical matrix through the linear response of electron density[26]. A $5\times5\times1$ supercell with $5\times5\times1$ **k**-mesh is used to ensure the convergence. The phonon dispersion is obtained using the Phonopy code with the harmonic IFCs as input[27].

Table 1 Calculated lattice parameters and band gap of monolayer MX_2. Experimental data are also given in parentheses for comparison.

	MoS_2	$MoSe_2$	WS_2
a (Å)	3.165 (3.160[29])	3.300 (3.288[29])	3.163 (3.154[30])
E_g (eV)	1.81 (1.88[31])	1.56 (1.57[32])	1.97 (1.95[33])

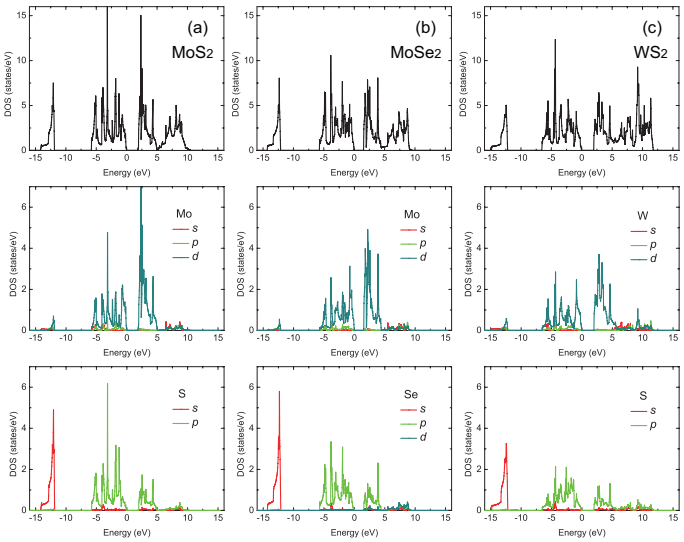

Fig. 2 Total and atom projected DOS for (a)MoS_2, (b)$MoSe_2$, and (c)WS_2.

3 Results and discussion

3.1 Crystal structures and interatomic bonding

Monolayer MX_2 has honeycomb structure with space group $P\bar{6}m2$[28], as shown in fig. 1. An M atom layer is sandwiched between two X atom layers, connected by covalent bonds. Each M atom is coordinated to six X atoms. The optimized lattice parameters of all studied MX_2 are shown in table 1. Our GGA calculations overestimate the lattice parameters by 0.16%, 0.36%, and 0.29%, respectively, which is a general feature of the GGA functional.

The electronic structures of all studied MX_2 are calculated by DFT method. As shown in table 1, the calculated band gap is consistent with the measurements[31–33]. The total and atom projected density of states (DOS) are shown in fig. 2. The valence band from -7 to 0 eV is mainly composed of M-d and X-p states, and the bands on each side of the band gap originate primarily from M-d state, which is in agreement with previous work[4]. The conduction band minimum from 0 to 5 eV mainly originates from M-d states, together with a small contribution of X-p states. Due to the less localized DOS of W atoms, the overlap between W-d and S-p states in both valence and conduction bands of WS_2 from -7 to 12 eV is larger than the other two materials, indicating a

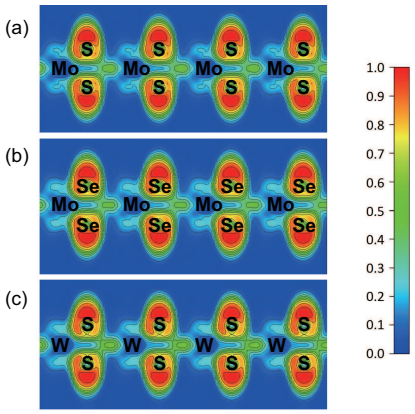

Fig. 3 ELF profiles of (a)MoS_2, (b)$MoSe_2$, and (c)WS_2 in the $[\bar{1}10]$ plane.

strong hybridization between W-*d* and S-*d* orbitals.

To explore the bonding characteristics of all studied MX_2, the electron localization function (ELF)[34–37] is investigated. The ELF is a position dependent function with values that range from 0 to 1. ELF=1 corresponds to perfect localization and ELF=0.5 corresponds to the electron-gas like pair probability. Fig. 3 presents the ELF profile of all studied MX_2 in the $[\bar{1}10]$ plane. The electrons are localized at X atoms, and are depleted at M atoms, suggesting that the electrons are transferred from M cations to X anions. Fig. 3 also indicates that MX_2 has both covalency and ionicity in the M-X bond, which compete with each other: with increasing nucleon number of both M and X atoms, the covalency of the M-X bond increases, while the ionicity of the M-X bond decreases[20]. In fact, the strength of the M-X bonding increases (decreases) with increasing the cation (anion) nucleon number[13,20]. Therefore, the W-S bonding is the strongest. The interatomic bonding will further affect the heat transport in these three materials.

3.2 Debye temperatures: Roles of mass and interatomic bonding

The phonon spectra of all studied MX_2 structures are calculated using the supercell approach, with the real-space force-constants calculated in the density-functional perturbation theory (DFPT)[26] within the Phonopy code[27]. Fig. 4 presents the phonon spectrum along several high symmetry directions, together with the corresponding projected phonon density of states (PDOS). The primitive cell of monolayer MX_2 contains 3 atoms, corresponding to three acoustic and six optical phonon branches.

The average atomic mass of all studied MX_2 are shown in table 2, as well as the mass ratio m_M/m_{2X}. The phonon frequency in fig. 4 decreases with increasing mass. The largest phonon frequencies of MoS_2, $MoSe_2$, and WS_2 are 461.6 cm^{-1}, 345.2 cm^{-1}, 432.8 cm^{-1}, respectively. It should be noted that, although $MoSe_2$ and WS_2 have similar average atomic mass, the optical phonon

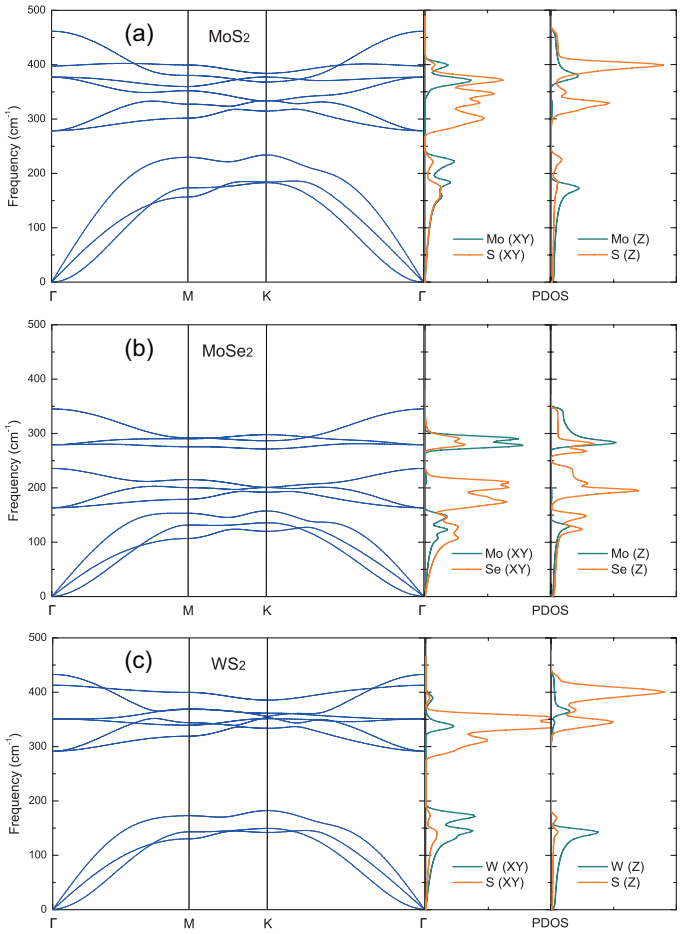

Fig. 4 Phonon spectrum and projected PDOS for (a)MoS_2, (b)$MoSe_2$, and (c)WS_2.

frequency of WS_2 is much higher than that of $MoSe_2$, since the optical phonon frequency is more sensitive to the anion mass m_{2X} than the cation mass m_M[20].

The average acoustic Debye temperature for monolayer MX_2 is determined from[38]

$$\frac{1}{\theta_D^3} = \frac{1}{2}\left(\frac{1}{\theta_{\mathrm{LA}}^3} + \frac{1}{\theta_{\mathrm{TA}}^3}\right), \quad (1)$$

where θ_i for each acoustic branch i (i = LA, TA) is defined as

$$\theta_i = \frac{\hbar\omega_{i,max}}{k_B}, \quad (2)$$

where $\hbar$ is Planck constant, $\omega_{i,max}$ is the phonon frequency at the zone boundary of the i-th acoustic mode, and k_B is Boltzmann constant. The calculated Debye temperatures θ_D for MoS_2, $MoSe_2$, and WS_2 are 262.3 K, 177.6 K, and 213.6 K, respectively, which are in good agreement with previous results, *i.e.* 260-320 K for MoS_2 estimated from specific-heat measurement[39],

Table 2 The average atomic mass $\overline{M}$, mass ratio m_M/m_{2X}, and Debye temperature θ_D of all studied MX_2.

Structure	$\overline{M}$ (amu)	m_M/m_{2X}	θ_D (K)
MoS_2	53.36	1.50	262.3
$MoSe_2$	84.63	0.61	177.6
WS_2	82.66	2.87	213.6

197.3±6.6 K for $MoSe_2$ estimated from photoconductivity measurements[40], 210 K for WS_2 estimated from the Lindemann formula[41].

As we mentioned above, low average atomic mass $\overline{M}$ and strong interatomic bonding will lead to a high Debye temperature. The average atomic mass plays a more important role in determining the Debye temperatures of MoS_2 and WS_2. For MoS_2 and $MoSe_2$, it is found that the $\overline{M}$ of MoS_2 is approximately two thirds the $\overline{M}$ of $MoSe_2$, and the calculated θ_D of MoS_2 is about 1.5 times larger than that of $MoSe_2$. For WS_2 and $MoSe_2$ which have similar mass, the effect of interatomic bonding is crucial in determining the Debye temperatures. The strong covalent W-S bonding in WS_2 can result in a relatively higher Debye temperature as compared to $MoSe_2$.

3.3 Phonon vibrational properties

Concerning thermal vibrations, the Debye temperature is a measure of the temperature above which all modes begin to be excited and below which modes begin to be frozen out[42]. We also investigate the vibrational properties of all studied MX_2 by calculating the projected PDOSs for the M(XY), M(Z), X(XY), and X(Z) vibrations as shown in fig. 4. Similar to the diatomic linear chain model, the scale of the acoustic (optical) phonon branch is dominated by atoms with larger (smaller) mass in three materials. As the mass ratio of all studied MX_2 (m_M/m_{2X}) in table 2 show, the acoustic phonon vibration in the PDOS is governed by the larger mass. Therefore the weight of M (X) atoms in the acoustic branch increases with increasing m_M (m_X). The mass ratio of MoS_2 is most close to 1, while that of WS_2 is much larger 1. Therefore the low-frequency acoustic phonon branches of MoS_2 up to 233.9 cm^{-1} are mainly from the Mo(XY), Mo(Z) and S(XY) vibrations due to similar mass, whereas those of WS_2 up to 182.3 cm^{-1} are mainly from the W(XY) and W(Z) vibrations due to the much larger mass of W atoms. In contrast to other two materials, the mass of transition metal atoms in $MoSe_2$ is smaller than the mass of chalcogenide atoms. Thus, although all Mo(XY), Mo(Z), Se(XY), and Se(Z) vibrations contribute significantly to the low-frequency branches of $MoSe_2$ up to 157.5 cm^{-1}, the PDOS of the Se(XY) and Se(Z) vibrations is higher than other two vibrations due to the relatively larger mass of Se atoms.

In addition, we investigate the vibrational mode of all studied MX_2 through the group-theoretical analysis. Since the monolayer

Table 3 Theoretical determined optical phonon frequencies (cm^{-1}) at the Γ point. The experimental results are also given in parentheses for comparison.

Structure	E''	E'	A_1'	A_2''
MoS_2	278.4	377.2	397.7	461.6
	(283[45])	(385[45])	(404[45])	(470[46])
$MoSe_2$	163.3	235.7	279.3	345.2
	(167[47])	(240[47])	(282[47])	(351[47])
WS_2	291.6	350.8	413.0	432.8
	(298[45])	(357[45])	(419[45])	(438[44])

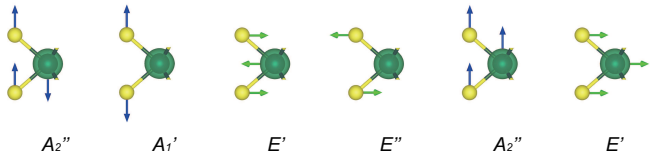

Fig. 5 Schematic phonon vibrations in MX_2.).

MX_2 belongs to the D_{3h} point group, the optical lattice-vibration modes at Γ point can be thus decomposed as

$$\Gamma_{optical} = A_2''(\mathrm{IR}) + A_1'(\mathrm{R}) + E'(\mathrm{IR}+\mathrm{R}) + E''(\mathrm{R}), \quad (3)$$

where IR and R denote infrared- and Raman-active mode respectively. Table 3 lists the optical phonon frequencies at the Γ point. The calculated phonon frequencies are in agreement with the experimental results, and the discrepancy is less than 3%. The LO/TO splitting is very small and can be neglected here[43,44].

The schematic vibrations for the phonon modes are shown in fig. 5, where one A_2'' and one E' are acoustic modes, the other A_2'' (E') is IR (both IR and R) active as shown in Eq. (3). A_2'' and A_1' modes vibrate along the z-direction, and E' and E'' modes vibrate in the $x-y$ direction. As shown before in fig. 4, in the case of $E'(\mathrm{LA/TA})$ in monolayer MoS_2, the Mo and S atoms vibrate with similar amplitudes; for $A_2''(\mathrm{ZA})$ in MoS_2, the vibrations of Mo atoms have much larger amplitudes. For both $E'(\mathrm{LA/TA})$ and $A_2''(\mathrm{ZA})$ in monolayer $MoSe_2$, the Se atoms vibrate with greater amplitudes than Mo atoms. The vibration of W atoms dominates both $E'(\mathrm{LA/TA})$ and $A_2''(\mathrm{ZA})$ vibrational modes in monolayer WS_2 due to the large m_W/m_{2S}.

3.4 Grüneisen parameter

The Grüneisen parameter γ, which describes the thermal expansion of a crystal on its vibrational properties, provides information on the anharmonic interactions. A larger Grüneisen parameter indicates stronger anharmonic vibrations. The expression for the Grüneisen parameter is given by[48,49]

$$\gamma = \frac{3\alpha B V_m}{C_V}, \quad (4)$$

Table 4 Comparison between the calculated and measured bulk modulus B (GPa), linear thermal expansion coefficient α (10^{-6} K^{-1}), and isometric heat capacity C_V (J mol^{-1} K^{-1}). The experimental results are also given in parentheses.

Structure	B	α	C_V
MoS_2	52.3	17.4	62.97
	(53.4±1.0[53])	(10.7[56])	(63.55[50])
	-	(82[47])	-
$MoSe_2$	57.3	19.5	68.75
	(45.7±0.3[54])	(7.24[57])	(68.60[51])
	(62[55])	(105[47])	-
WS_2	77.9	14.8	63.49
	(61±1[58])	(6.35[30])	(63.8±0.3[52])

where α is the linear thermal expansion coefficient, B is the bulk modulus, V_m is the molar volume, and C_V is the isometric heat capacity.

Table 4 compares the calculated bulk modulus, linear thermal expansion coefficient, and isometric heat capacity with experimental results at 300 K. The bulk modulus B and linear thermal expansion coefficient α are calculated using the quasi-harmonic approximation (QHA), which takes the first-order anharmonicity into account[27]. The obtained B for MoS_2 is in agreement with the experimental value[53]. For $MoSe_2$, the computed B is in the range of measured values[54,55]. Great discrepancies between the calculated and experimental B are present for WS_2. The bulk modulus is used to describe the stiffness of MX_2[20]. Since WS_2 is found to have larger bulk modulus, the bonding in WS_2 appears to be much stronger comparing to other two materials. The calculated α for MoS_2 and $MoSe_2$ at 300 K are in the range of measured values[47,56,57], while the calculated α is larger than the measured one for WS_2.

The isometric heat capacity can be calculated as

$$C_V = \left(\frac{\partial E}{\partial T}\right)_V = \sum_{n,\mathbf{q}} k_B \left(\frac{\hbar\omega_n(\mathbf{q})}{k_B T}\right)^2 \frac{e^{\hbar\omega_n(\mathbf{q})/k_B T}}{(e^{\hbar\omega_n(\mathbf{q})/k_B T} - 1)^2}, \quad (5)$$

where T is temperature, and $\omega_n(\mathbf{q})$ is the phonon frequency of the n-th branch with wave vector $\mathbf{q}$. The calculated values of C_V for MoS_2, $MoSe_2$, and WS_2 at room temperature are in good agreement with the experimental results[50–52].

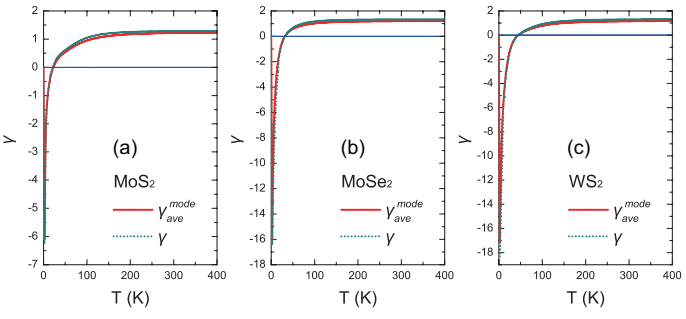

Fig. 6 Calculated temperature-dependent Grüneisen parameter for (a)MoS_2, (b)$MoSe_2$ and (c)WS_2.

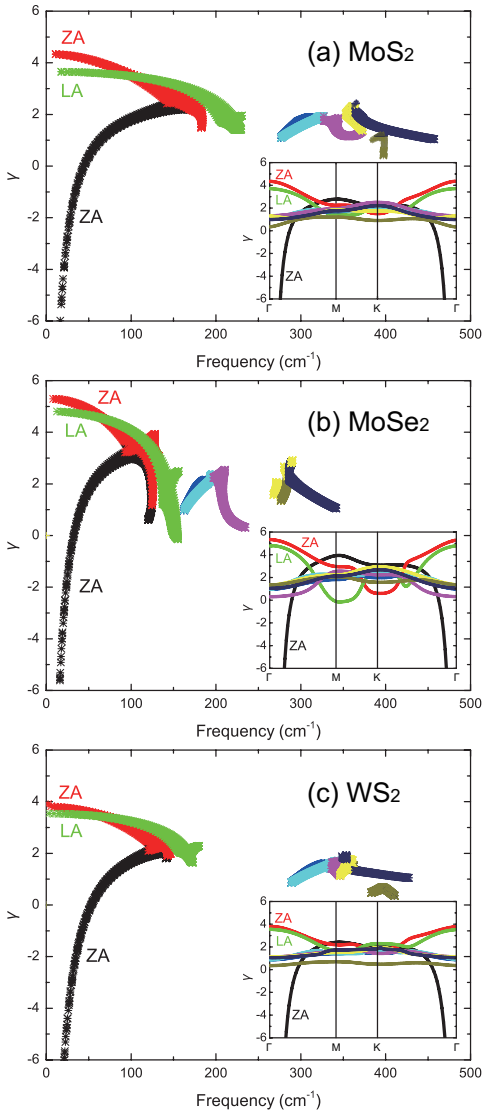

Fig. 7 Calculated mode Grüneisen parameter for (a)MoS_2, (b)$MoSe_2$ and (c)WS_2 with respect to frequencies, and with respect to wave vectors as shown in the inset.

As shown in fig. 6, the temperature-dependent Grüneisen parameter is calculated using Eq. (4). The Grüneisen parameter can also be calculated by averaging the mode Grüneisen parameter $\gamma_n(\mathbf{q})$,

$$\gamma_{ave}^{mode} = \frac{1}{C_V} \sum_{n,\mathbf{q}} \gamma_n(\mathbf{q}) C_{V,n}(\mathbf{q}), \quad (6)$$

where $C_{V,n}(\mathbf{q})$ is the mode heat capacity. The mode Grüneisen

parameter is given by

$$\gamma_n(\mathbf{q}) = -\frac{a_0}{\omega_n(\mathbf{q})}\frac{\partial \omega_n(\mathbf{q})}{\partial a}, \quad (7)$$

where a_0 is the equilibrium lattice constant at 0 K. Fig. 6 also shows the calculated γ_{ave}^{mode}, which is consistent with the Grüneisen parameter calculated using Eq. (4).

The frequency dependence of mode Grüneisen parameter of MoS_2 in the irreducible BZ is plotted in fig. 7, and the mode Grüneisen parameter along symmetry directions is shown in the inset. Similar to diamond, graphite and graphene[59], negative γ_{ZA} is observed at low frequencies (less than 50 cm^{-1} in MoS_2, 30 cm^{-1} in $MoSe_2$ and 50 cm^{-1} in WS_2), which originates from the low lattice dimensionality. The average Grüneisen parameter is negative at low temperatures in fig. 6 because only the low-frequency ZA phonons are excited. At higher temperatures, the excitation of other positive-γ modes results in positive γ_{ave}^{mode}. Our results are in agreement with previous calculations[60–62]. The calculated γ_{ave}^{mode} at room temperature are 1.22, 1.20 and 1.15 for MoS_2, $MoSe_2$, and WS_2, respectively, indicating the high anharmonicity of MoS_2, while the anharmonicity of WS_2 is weak.

3.5 Thermal conductivity

Assuming that only the acoustic phonon modes participate in the heat conduction process, the lattice thermal conductivity in the temperature range where three-phonon scattering is dominant, as derived by Slack[16,38], is given as following,

$$\kappa_l = A\frac{\overline{M}\theta_D^3\delta n^{1/3}}{\gamma^2 T}, \quad (8)$$

where δ^3 is the volume per atom, n is the number of atoms in the primitive unit cell, and A is a constant which is given by[63]

$$A = \frac{2.43\times10^{-6}}{1-0.514/\gamma+0.228/\gamma^2} \quad (9)$$

when the units of κ_l, $\overline{M}$, and δ are taken as W/mK, amu, and Å, respectively. The obtained lattice thermal conductivities for monolayer MoS_2, $MoSe_2$, and WS_2 at room temperature are 33.6 W/mK, 17.6 W/mK and 31.8 W/mK, respectively, which are in good agreement with the experimental value of 34.5 ± 4 W/mK for monolayer MoS_2[14], and 32 W/mK for monolayer WS_2[15]. Although there is no experimental value for monolayer $MoSe_2$, our calculated κ_l is a reasonable prediction.

The factor $\overline{M}\theta_D^3\delta$ and A/γ^2 in Eq. (8) are crucial to understand the thermal transport in MoS_2, $MoSe_2$, and WS_2. The Slack's expression attempts to normalize the effect of mass density, crystal structure, interatomic bonding, and anharmonicity[16–18]. The factor $\overline{M}\theta_D^3\delta$ in Eq. (8) is maximized for light mass, strong bonded crystals, because low average atomic mass and strong interatomic bonding lead to a large θ_D^3, and the θ_D^3 term dominates the overall behaviour[16]. The Debye temperature reflects the magnitude of sound velocity. Higher Debye temperature means increased phonon velocities, and increased acoustic-phonon frequencies as mentioned above, which suppress phonon-phonon scattering by decreasing phonon populations[17]. The factor A/γ^2 in Eq. (8) implies that high thermal conductivity is correlated to low anharmonicity (small γ).

Our results suggest that the average atomic mass plays a key role in determining the phonon dispersion of MoS_2 and WS_2, and subsequently determines the Debye temperature. MoS_2 with much lower average atomic mass has higher Debye temperature, which results in a higher thermal conductivity.

As compared to $MoSe_2$, although WS_2 has similar average atomic mass, the strong W-S bonding leads to a higher Debye temperature. Furthermore, small γ of WS_2 means low anharmonicity, which also results in a higher thermal conductivity. Therefore the thermal conductivity of WS_2 is determined by the competition between high average atomic mass, strong covalent W-S bonding and low anharmonicity.

4 Conclusion

In summary, we investigate the lattice dynamics and thermodynamic properties of MoS_2, $MoSe_2$, and WS_2 by first principles calculations. The obtained phonon frequencies and lattice thermal conductivity agree well with experimental measurements. Our calculations show that the thermal conductivity of MoS_2 is highest among the three materials due to its largest Debye temperature, which is attributed to the lowest average atomic mass. We also find that the stronger W-S bonding and lower anharmonicity of WS_2 lead to a much higher thermal conductivity compared to $MoSe_2$.

Acknowledgement

This work is in part supported by the National Natural Science Foundation of China under Grants No. 11374063 and 11404348, 973 Program (No. 2013CAB01505), and Ningbo Science and Technology Innovation Team (Grant No. 2014B82004).

References

1 Ferrari A. C. *et. al.*, Nanoscale **7**, 4598 (2015).
2 J. Klinovaja and D. Loss, Phys. Rev. B **88**, 075404 (2013).
3 M. Buscema, M. Barkelid, V. Zwiller, H. S. J. van der Zant, G. A. Steele, and A. Castellanos-Gomez, Nano Letters **13**, 358 (2013).
4 A. Kumar and P. Ahluwalia, The European Physical Journal B **85**, 186 (2012).
5 J. Lin, J. Zhong, S. Zhong, H. Li, H. Zhang, and W. Chen, Applied Physics Letters **103**, 063109 (2013).
6 D. Sarkar, W. Liu, X. Xie, A. C. Anselmo, S. Mitragotri, and K. Banerjee, ACS Nano **8**, 3992 (2014).

7 A. Splendiani, L. Sun, Y. Zhang, T. Li, J. Kim, C.-Y. Chim, G. Galli, and F. Wang, Nano Letters **10**, 1271 (2010).

8 H. Sahin, S. Tongay, S. Horzum, W. Fan, J. Zhou, J. Li, J. Wu, and F. M. Peeters, Phys. Rev. B **87**, 165409 (2013).

9 S. Horzum, H. Sahin, S. Cahangirov, P. Cudazzo, A. Rubio, T. Serin, and F. M. Peeters, Phys. Rev. B **87**, 125415 (2013).

10 S. Tongay, J. Zhou, C. Ataca, K. Lo, T. S. Matthews, J. Li, J. C. Grossman, and J. Wu, Nano Letters **12**, 5576 (2012).

11 H. Zeng, J. Dai, W. Yao, D. Xiao, and X. Cui, Nat Nano **7**, 490 (2012).

12 J. M. Ziman, *Electrons and Phonons: The Theory of Transport Phenomena in Solids* (Oxford University Press, 1960).

13 X. Gu and R. Yang, Applied Physics Letters **105**, 131903 (2014).

14 R. Yan, J. R. Simpson, S. Bertolazzi, J. Brivio, M. Watson, X. Wu, A. Kis, T. Luo, A. R. Hight Walker, and H. G. Xing, ACS Nano **8**, 986 (2014).

15 N. Peimyoo, J. Shang, W. Yang, Y. Wang, C. Cong, and T. Yu, Nano Research **8**, 1210 (2015).

16 G. A. Slack, Journal of Physics and Chemistry of Solids **34**, 321 (1973).

17 L. Lindsay, D. A. Broido, and T. L. Reinecke, Phys. Rev. Lett. **111**, 025901 (2013).

18 A. Jain and A. J. McGaughey, Journal of Applied Physics **116**, 073503 (2014).

19 K. H. Michel, S. Costamagna, and F. M. Peeters, Phys. Rev. B **91**, 134302 (2015).

20 L.-F. Huang and Z. Zeng, The Journal of Physical Chemistry C **119**, 18779 (2015).

21 M. Boukhicha, M. Calandra, M.-A. Measson, O. Lancry, and A. Shukla, Phys. Rev. B **87**, 195316 (2013).

22 A. L. C. da Silva, L. Cândido, J. N. T. Rabelo, G.-Q. Hai, and F. M. Peeters, EPL (Europhysics Letters) **107**, 56004 (2014).

23 Y. Gong, Z. Liu, A. R. Lupini, G. Shi, J. Lin, S. Najmaei, Z. Lin, A. L. Elías, A. Berkdemir, G. You, et al., Nano Letters **14**, 442 (2014).

24 D. O. Dumcenco, H. Kobayashi, Z. Liu, Y.-S. Huang, and K. Suenaga, Nat Commun **4**, 1351 (2013).

25 G. Kresse and J. Furthmüller, Phys. Rev. B **54**, 11169 (1996).

26 S. Baroni, S. de Gironcoli, A. Dal Corso, and P. Giannozzi, Rev. Mod. Phys. **73**, 515 (2001).

27 A. Togo, F. Oba, and I. Tanaka, Phys. Rev. B **78**, 134106 (2008).

28 A. Molina-Sánchez and L. Wirtz, Phys. Rev. B **84**, 155413 (2011).

29 R. Coehoorn, C. Haas, J. Dijkstra, C. J. F. Flipse, R. A. de Groot, and A. Wold, Phys. Rev. B **35**, 6195 (1987).

30 A. Matthäus, A. Ennaoui, S. Fiechter, S. Tiefenbacher, T. Kiesewetter, K. Diesner, I. Sieber, W. Jaegermann, T. Tsirlina, and R. Tenne, Journal of The Electrochemical Society **144**, 1013 (1997).

31 K. F. Mak, C. Lee, J. Hone, J. Shan, and T. F. Heinz, Phys. Rev. Lett. **105**, 136805 (2010).

32 P. Tonndorf, R. Schmidt, P. Böttger, X. Zhang, J. Börner, A. Liebig, M. Albrecht, C. Kloc, O. Gordan, D. R. T. Zahn, et al., Opt. Express **21**, 4908 (2013).

33 H. R. Gutiérrez, N. Perea-López, A. L. Elías, A. Berkdemir, B. Wang, R. Lv, F. López-Urías, V. H. Crespi, H. Terrones, and M. Terrones, Nano Letters **13**, 3447 (2013).

34 A. D. Becke and K. E. Edgecombe, J. Chem. Phys. **81**, 5397 (1990).

35 A. Savin, J. Flad, et al., Angewandte Chemie International Edition **31**, 187 (1992).

36 C. Gatti, Zeitschrift für Kristallographie **220**, 399 (2005).

37 K. Chen and S. Kamran, Modeling and Numerical Simulation of Material Science **3**, 7 (2013).

38 D. T. Morelli and J. P. Heremans, Applied Physics Letters **81**, 5126 (2002).

39 Y. S. Touloukian and E. H. Buyco, eds., *Specific Heat-Nonmetallic Solids, in Thermal Properties of Matter: The TPRC Data Series*, Vol. 5 (New York: Plenum, 1970).

40 S. Hu, Y. Lee, J. Shen, K. Chen, K. Tiong, and Y. Huang, Solid State Communications **139**, 176 (2006).

41 C. H. Ho, C. S. Wu, Y. S. Huang, P. C. Liao, and K. K. Tiong, Journal of Physics: Condensed Matter **10**, 9317 (1998).

42 T. Nakashima and Y. Umakoshi, Philosophical Magazine Letters **66**, 317 (1992).

43 Y. Cai, J. Lan, G. Zhang, and Y.-W. Zhang, Phys. Rev. B **89**, 035438 (2014).

44 R. D. Luttrell, S. Brown, J. Cao, J. L. Musfeldt, R. Rosentsveig, and R. Tenne, Phys. Rev. B **73**, 035410 (2006).

45 X. Zhang, X.-F. Qiao, W. Shi, J.-B. Wu, D.-S. Jiang, and P.-H. Tan, Chem. Soc. Rev. **44**, 2757 (2015).

46 T. J. Wieting and J. L. Verble, Phys. Rev. B **3**, 4286 (1971).

47 D. J. Late, S. N. Shirodkar, U. V. Waghmare, V. P. Dravid, and C. N. R. Rao, Chem. Phys. Chem. **15**, 1592 (2014).

48 G. Grimvall, *Thermophysical properties of materials* (Amsterdam: Elsevier, 1999).

49 H. Shao, X. Tan, T. Hu, G.-Q. Liu, J. Jiang, and H. Jiang, EPL (Europhysics Letters) **109**, 47004 (2015).

50 L. S. Volovik, V. V. Fesenko, A. S. Bolgar, S. V. Drozdova, L. A. Klochkov, and V. F. Primachenko, Soviet Powder Metallurgy and Metal Ceramics **17**, 697 (1978).

51 A. S. Blinder, A. V. Bolgar and Z. A. Trofimova, Powder Metallurgy and Metal Ceramics **32**, 234 (1993).

52 P. A. G. O'hare, W. Hubbard, G. Johnson, and H. Flotow, The

Journal of Chemical Thermodynamics **16**, 45 (1984).

53 R. Aksoy, Y. Ma, E. Selvi, M. Chyu, A. Ertas, and A. White, Journal of Physics and Chemistry of Solids **67**, 1914 (2006).

54 R. Aksoy, E. Selvi, and Y. Ma, Journal of Physics and Chemistry of Solids **69**, 2138 (2008).

55 Z. Zhao, H. Zhang, H. Yuan, S. Wang, Y. Lin, Q. Zeng, G. Xu, Z. Liu, G. K. Solanki, K. D. Patel, et al., Nat Commun **6**, 7312 (2015).

56 E. M. Dudnik and O. V. Kh., Soviet Powder Metallurgy and Metal Ceramics **5**, 125 (1966).

57 S. H. El-Mahalawy and B. L. Evans, J. Appl. Crystallogr. **9**, 403 (1976).

58 E. Selvi, Y. Z. Ma, R. Aksoy, A. Ertas, and A. White, Journal of Physics and Chemistry of Solids **67**, 2183 (2006).

59 N. Mounet and N. Marzari, Phys. Rev. B **71**, 205214 (2005).

60 L. F. Huang, P. L. Gong, and Z. Zeng, Phys. Rev. B **90**, 045409 (2014).

61 C. Sevik, Phys. Rev. B **89**, 035422 (2014).

62 B. Peng, H. Zhang, H. Shao, X. Zhang, and H. Zhu, arXiv: **1508**, 03435 (2015).

63 C. L. Julian, Phys. Rev. **137**, A128 (1965).

Graphical Abstract

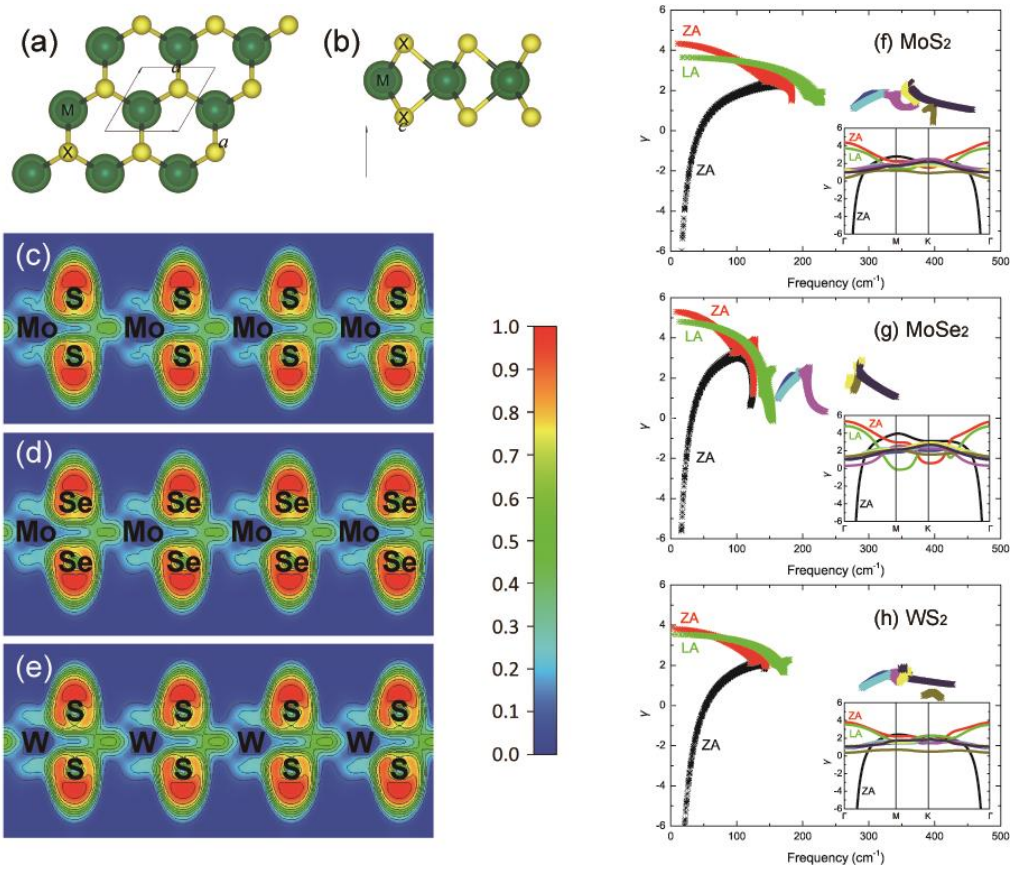

The present work shows that the thermal conductivity of MoS_2 is largest among the three MX_2 (Figs. a-b) materials due to its largest Debye temperature, which is attributed to the lowest average atomic mass, and WS_2 has stronger W-S bonding (ELF profile in Fig. e) and lower anharmonicity (Fig. h), leading to a much larger thermal conductivity of WS_2 compared to $MoSe_2$.